



# Depth-varying seismogenesis on an oceanic detachment fault at 13°20'N on the Mid-Atlantic Ridge



Timothy J. Craig<sup>a,\*</sup>, Ross Parnell-Turner<sup>b</sup>

<sup>a</sup> Institute of Geophysics and Tectonics, School of Earth and Environment, University of Leeds, Leeds, LS2 9JT, UK

<sup>b</sup> Department of Geology and Geophysics, Woods Hole Oceanographic Institution, Woods Hole Road, Woods Hole, MA 02543, USA

## ARTICLE INFO

### Article history:

Received 1 July 2017

Received in revised form 31 August 2017

Accepted 8 September 2017

Available online xxx

Editor: R. Bendick

### Keywords:

detachment fault  
seismicity  
mid-ocean ridge  
rheology

## ABSTRACT

Extension at slow- and intermediate-spreading mid-ocean ridges is commonly accommodated through slip on long-lived faults called oceanic detachments. These curved, convex-upward faults consist of a steeply-dipping section thought to be rooted in the lower crust or upper mantle which rotates to progressively shallower dip-angles at shallower depths. The commonly-observed result is a domed, sub-horizontal oceanic core complex at the seabed. Although it is accepted that detachment faults can accumulate kilometre-scale offsets over millions of years, the mechanism of slip, and their capacity to sustain the shear stresses necessary to produce large earthquakes, remains subject to debate. Here we present a comprehensive seismological study of an active oceanic detachment fault system on the Mid-Atlantic Ridge near 13°20'N, combining the results from a local ocean-bottom seismograph deployment with waveform inversion of a series of larger teleseismically-observed earthquakes. The unique coincidence of these two datasets provides a comprehensive definition of rupture on the fault, from the uppermost mantle to the seabed. Our results demonstrate that although slip on the deep, steeply-dipping portion of detachment faults is accommodated by failure in numerous microearthquakes, the shallow, gently-dipping section of the fault within the upper few kilometres is relatively strong, and is capable of producing large-magnitude earthquakes. This result brings into question the current paradigm that the shallow sections of oceanic detachment faults are dominated by low-friction mineralogies and therefore slip aseismically, but is consistent with observations from continental detachment faults. Slip on the shallow portion of active detachment faults at relatively low angles may therefore account for many more large-magnitude earthquakes at mid-ocean ridges than previously thought, and suggests that the lithospheric strength at slow-spreading mid-ocean ridges may be concentrated at shallow depths.

© 2017 Elsevier B.V. All rights reserved.

## 1. Introduction

Earthquake activity at mid-ocean ridges provides an insight into the thermal and rheological state of the lithosphere as it is created and subsequently deformed (e.g. Sykes, 1967). At slow-spreading ridges, a significant portion of plate separation may be accommodated by slip on long-lived detachment faults, which are thought to initiate at steep dips and then roll over to become sub-horizontal at the seafloor (Cann et al., 1997; Morris et al., 2009). This process leads to the exhumation of lower crustal and upper mantle rocks at the seabed, which often form kilometre-scale domes called oceanic core complexes (OCCs; Tucholke et al., 1998; MacLeod et al., 2002; Dick et al., 2008; Escartin and Canales, 2011).

While seafloor mapping and sampling, and active-source seismic imaging provide a static picture of these features (e.g. Dick, 1989; Cann et al., 1997; Blackman et al., 2009), the subsurface mechanics of the process of roll-over remains enigmatic. Short-duration local ocean bottom seismograph (OBS) experiments have shown that microearthquakes in these settings consistently occur at depths between 3 and 7 km below seafloor (bsf; Toomey et al., 1985; Kong et al., 1992; Wolfe et al., 1995; Grevemeyer et al., 2013). Some of these earlier studies lacked the high-resolution bathymetry necessary to identify detachment faults prior to deployment, and hence used networks not optimised for studying earthquakes associated with these faults. Two deployments of densely-spaced OBS networks specifically targeting identified active core complexes in the North Atlantic Ocean have shown that the pattern of microearthquakes defines a steep-dipping planar normal fault surface at depth. However rupture at depths shallower than 4 km bsf remains undetected (deMartin et al., 2007; Parnell-Turner et al., 2017). This apparent lack of shallow seis-

\* Corresponding author.

E-mail address: t.j.craig@leeds.ac.uk (T.J. Craig).

micity has been suggested to be the result of fractured, permeable crust being incapable of supporting sufficient stresses to produce earthquakes, or the presence of hydrothermally-altered fault gouge material leading to aseismic slip (deMartin et al., 2007; Grevemeyer et al., 2013). In contrast, continental detachment faults associated with metamorphic core complexes, for example in Papua New Guinea, may be capable of hosting large-magnitude, shallowly-dipping normal faulting earthquakes on their uppermost sections (Abers, 1991; Abers et al., 1997), although recent geodetic work instead suggests much of the slip may be accommodated aseismically (Wallace et al., 2014).

A large proportion of the slow-spreading Mid-Atlantic Ridge (MAR) shows evidence for detachment faulting and the accretion of oceanic crust through OCC formation (Smith et al., 2006; Escartín et al., 2008). Studies of teleseismically-detected earthquakes at slow-spreading ridges have shown that events in the median valley have typical focal depths of 1–4 km bsf, and dip angles of  $\sim 45^\circ$  (Huang et al., 1986), consistent with global surveys of large earthquakes at other slow-spreading ridges (Jemsek et al., 1986; Solomon and Huang, 1987). Lacking the constraints necessary to relate these earthquakes to a particular fault, they have been assumed to be related to planar rift-border faults, and not to be associated with detachment faulting. This assumption, however, contrasts with evidence that detachment-dominated segments of the Mid-Atlantic Ridge generate more earthquakes in both teleseismic and hydroacoustic catalogues (Escartín et al., 2008; Olive and Escartín, 2016), suggesting a link between the presence of detachment faulting and the production of large mid-ocean ridge earthquakes.

Hence, three apparently disparate modes of detachment fault behaviour have been identified seismologically. First, dominantly aseismic, uncoupled behaviour is expected for oceanic detachments associated with weak, low friction mineralogies; second, high-moment-release, teleseismically-detected earthquakes are observed along sections of detachment-fault dominated mid-ocean ridge segments; and third, large-magnitude earthquakes are associated with detachment faulting bounding metamorphic core complexes on the continents. In an attempt to characterise the full seismogenic behaviour of a detachment fault across the complete range of observational scales, we consider the seismicity associated with an actively slipping oceanic detachment fault on the MAR near  $13^\circ 20' N$ , integrating the results from a local OBS deployment with observations of co-located large earthquakes from the global seismic network.

## 2. Seismicity near the $13^\circ 20' N$ detachment

We focus on the area near  $13^\circ 20' N$  on the MAR, where an active OCC has been previously extensively surveyed and sampled (Smith et al., 2006; MacLeod et al., 2009; Mallows and Searle, 2012; Escartín et al., 2017; Bonnemains et al., 2017). The exposed fault surface has prominent spreading-parallel corrugations, and is thought to record  $\sim 9$  km of heave since its initiation at  $\sim 0.4$  Ma (MacLeod et al., 2009; Mallows and Searle, 2012).

In 2014, an array of 25 OBSs detected  $\sim 240,000$  microearthquakes near the  $13^\circ 20' N$  detachment fault over a period of six months (Parnell-Turner et al., 2017). There are two domains of seismicity: reverse-faulting earthquakes beneath the dome at 3–7 km bsf, attributed to internal compression within the bending footwall; and normal-faulting earthquakes towards the centre of the axial valley, at depths of 5–12 km bsf (Fig. 1 and histograms in Figs. 4a and 5). The along-axis pattern of normal-faulting microearthquakes suggests that at depth, the active detachment fault extends beyond the limits of the exposed corrugated surface. These normal faulting earthquakes have a composite focal mechanism indicating slip on a steeply eastward-dipping plane

(see Supplementary Table 1), interpreted to be the downdip portion of the detachment fault in the region where a coherent fault zone forms. The depth extent and apparent dip of normal-faulting microearthquakes is consistent with that observed at the active Trans-Atlantic Geotraverse (TAG) detachment near  $26^\circ N$  on the MAR (deMartin et al., 2007). The lack of shallow microearthquakes at these two locations means that the style of deformation (e.g., aseismic slip, or seismic failure in large or small earthquakes) on the shallow, roll-over portion of detachment faults remains uncertain.

Over the last decade, three large-magnitude, teleseismically-detected normal-faulting earthquakes have occurred in the vicinity of the  $13^\circ 20' N$  OCC. A  $M_w$  5.7 event that occurred on the 7th December 2008 (hereafter referred to as the 2008 mainshock) was followed a day later by a  $M_w$  5.5 aftershock, and a third event,  $M_w$  5.7, occurred on 20th October 2016. The ability to relate a given earthquake with a specific fault near the mid-ocean ridge is hampered by the uncertainty in earthquake location and the absence of near-field data. In order to overcome this limitation, we seek to determine the most likely hypocentral location for these three events, and therefore their relationship to the local tectonic structures, by evaluating five possible scenarios. First, that slip occurred on the shallow portion of the  $13^\circ 20' N$  detachment which lacks microearthquakes; second, that these events are co-located with microearthquakes on the steeper, deeper detachment surface; third, that these events are shallow antithetic events within the  $13^\circ 20' N$  detachment footwall block; fourth, that they represent breakup of the detachment hanging wall in the formation of rider blocks; or fifth, that they are unrelated to the  $13^\circ 20' N$  detachment fault and occurred on another fault nearby.

## 3. Constraints on earthquake location

Earthquake locations based on globally-observed travel times for these earthquakes indicate that they all occurred within 10 km of the active  $13^\circ 20' N$  detachment (Fig. 1, Table S2; International Seismological Centre 2014). In particular, the 2016 event co-locates with the  $13^\circ 20' N$  detachment, slightly up-dip of the observed microseismicity. Quoted catalogue uncertainties suggest that these locations are accurate to  $\sim \pm 10$  km [National Earthquake Information Center; NEIC], comparable to the mean error in global seismological hypocentre locations, based on geodetic calibration (Lohman and Simons, 2005; Weston et al., 2012). Independently calculated locations for these earthquakes from different agencies show a strong clustering within this level of uncertainty (see Fig. 1 and Table S1). Although absolute locations for these earthquakes are limited by the lack of any near-source data, improved data coverage between 2008 and 2016 suggests that the 2016 location is probably more reliable. Despite these improvements, attributing these events to specific tectonic structures, and relating them to one another, remains difficult.

We relocate the three teleseismically-observed earthquakes relative to one another using inter-event times determined using waveform cross-correlation (see Fig. 3). This approach refines inter-event distances, although it does not provide absolute locations relative to geographic features (such as the  $13^\circ 20' N$  OCC). Exploiting the broad-scale similarity in mechanism and source duration between the three teleseismically-observed earthquakes (see Section 4), we relocate them relative to each other on the basis of relative travel times derived from cross-correlation of the  $P$  and  $S$  waves. We use a correlation window of 45 s, starting 5 s before the predicted phase arrival time. Relative travel times are computed using all three components (vertical for the  $P$  wave, east and north for the  $S$  wave). We initially use all stations that cover the observation periods for at least two of the three events considered, and then limit the dataset based on the ability to visually

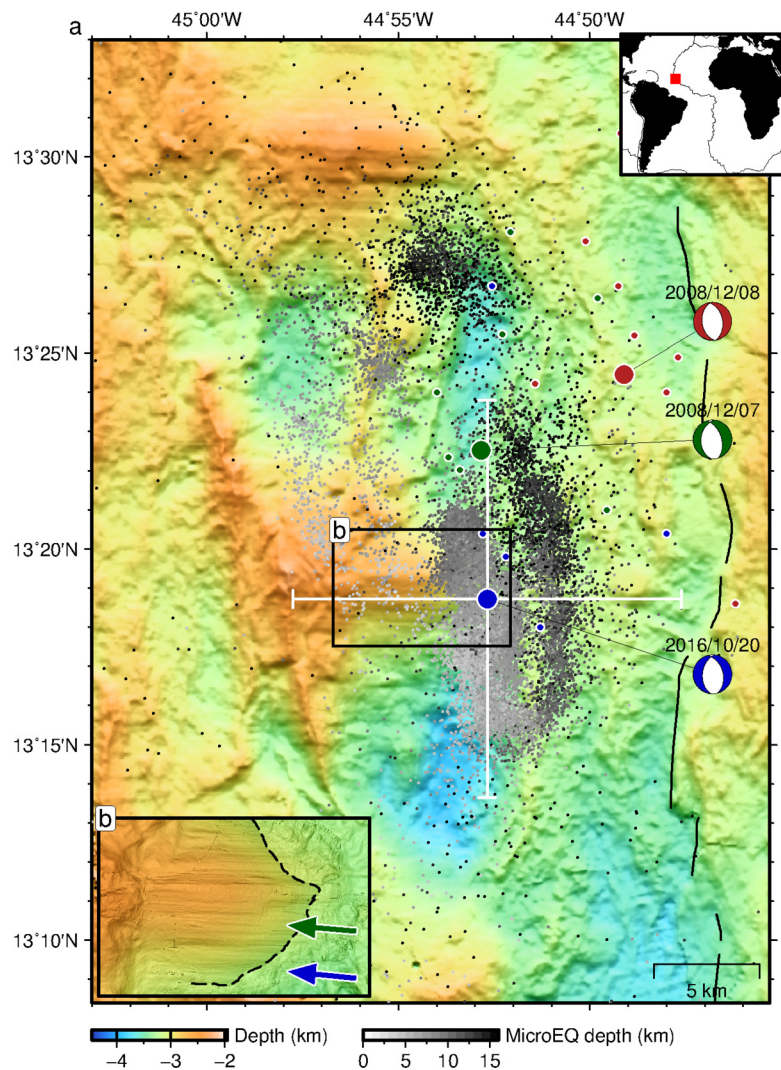


**Fig. 1.** Bathymetry and earthquakes. Inset: red box shows study location. (a) Small dots are microearthquakes shaded by depth (Parnell-Turner et al., 2017); large blue circle is preferred hypocentre for  $M_w$  5.7 event on 20th October 2016 (NEIC catalogue); large green/red circles are hypocentres for  $M_w$  5.6/5.5 events on 7th/8th December 2008 events, respectively (ISC catalogue); focal mechanisms shown are best fitting solutions from this study; small coloured circles are unfavoured hypocentres from alternative catalogues (see Table S1 for details); solid black line is eastern border fault (EBF); arrow tips mark small fault scarps near OCC. (b) Detailed view of corrugated fault surface, with 2 m resolution microbathymetry (Escartín et al., 2017, French Oceanographic Cruises, <http://dx.doi.org/10.17600/13030070>), blue/green arrows indicate slip direction of 2016/2008 main shocks, respectively; dashed line is hanging wall cutoff (HWC). (For interpretation of the references to colour in this figure legend, the reader is referred to the web version of this article.)

identify arrivals in the waveforms, and on the magnitude of the computed cross correlation coefficient, using a threshold value of 0.5. Fig. S1 shows the full station set used for  $P$  and  $S$  waves, overlain on the radiation pattern for the 2016 earthquake (those for 2008 are similar). Note that station coverage is not the same for all three earthquakes, leading to varying sets of station pairs for the three event-pairs possible. Whilst the majority of stations active in 2008 cover both of the earthquakes in this year, the smaller magnitude of the 8th December 2008 event leads to a smaller number of stations with clear arrivals for both events.

We use a tapered frequency band, optimised between 0.05 and 1 Hz, for the cross correlation. Expanding this band to incorporate higher frequencies initially leads to a similar location offset, but the inter-event coherence, particularly to the 2008 aftershock, decays rapidly above 1 Hz (demonstrated in Fig. 3), leading to a decrease in the number of reliable inter-event travel times. For the final set of relocations presented in Fig. 2, we use 309  $P$ -wave event-pairs, and 269  $S$ -wave pairs, with average cross-correlation coefficients of 0.75 and 0.85, respectively. Prior to relocation, the mean inter-event travel-time residual is 1.02 s. After relocation,

the residual decreases to 0.34 s (residual populations are shown in Fig. 2b, c).

We test the relocation results by limiting the dataset to those stations at epicentral distances of  $<30^\circ$  (32  $P$ -wave and 22  $S$ -wave pairs) which should be more sensitive to lateral offsets in location. This refinement leads to a similar set of relocations, where the 2008 mainshock and the 2016 event occur within one rupture length of each other ( $\sim 6$  km; see below). The 2008 aftershock is offset to the north and west, although there is some difference in the magnitude of the shift for this event (Fig. 2). Similarly, relocations using datasets limited to  $P$ -wave and  $S$ -wave arrivals alone (Fig. 2a) produces the same overall pattern across the three earthquakes, with the main variation in the distance, but not direction, of the offset to the 2008 aftershock.

Although hampered by scant near-source data (nearest stations  $>14^\circ$  epicentral distance), the relocations conclusively indicate that the 2008 mainshock and 2016 event (earthquakes of similar magnitude) occurred near to one another. Plate spreading rates in this area are unlikely to be sufficient to accumulate enough strain to produce a  $M_w$  5.7 earthquake in the 8-year inter-event period,

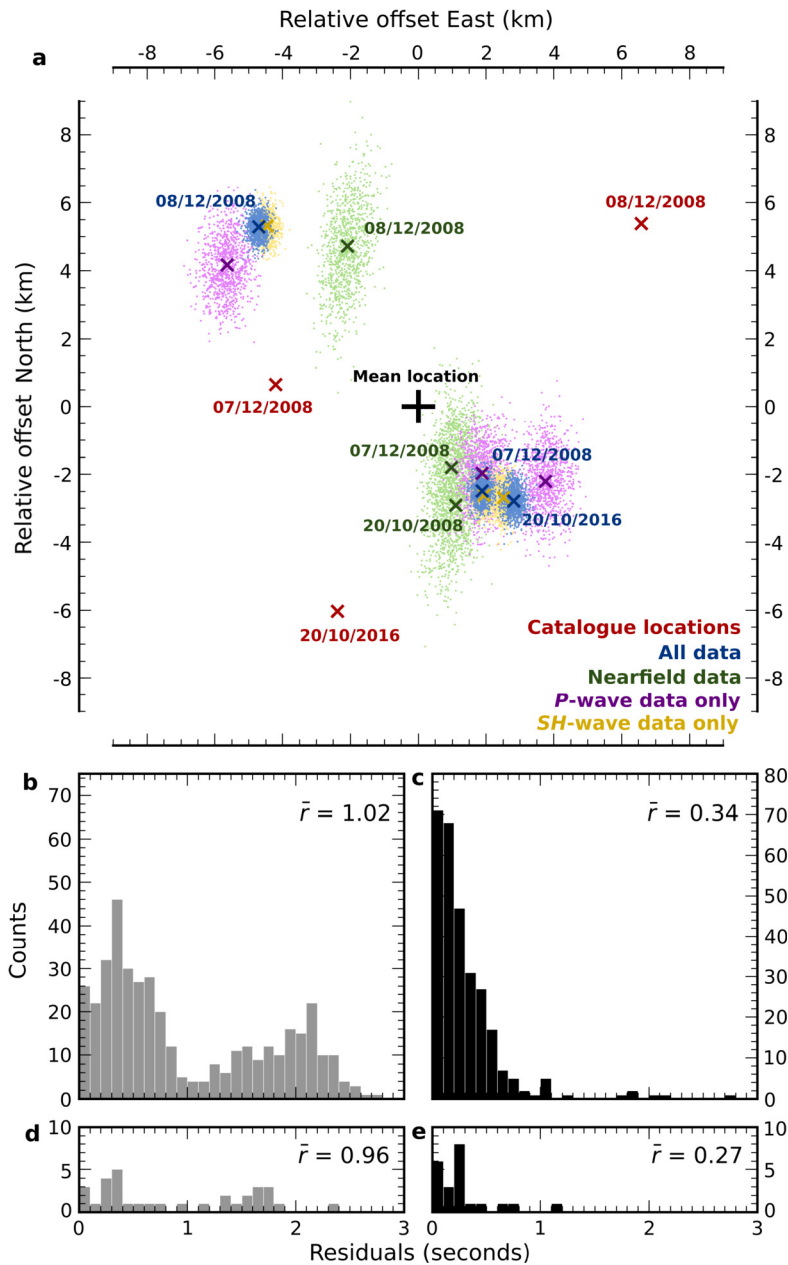


**Fig. 2.** Relative relocation of teleseismic earthquakes. (a) Relative earthquake locations for the three teleseismically-observed events. Sets of locations are shown relative to their common mean, defined as plot origin, shown by large black cross. Red crosses are initial catalogue locations. Blue crosses are locations after relocation using all data. Green crosses are relocations using only data at epicentral distances  $<30^\circ$ . Purple/yellow crosses are relocations using only *P*-wave/*SH*-wave data, respectively. Small coloured points show 1000 relocations after relative time dataset has been randomly perturbed based on a normal distribution of width defined by mean post-relocation residual. (b) Cross-correlation derived residuals prior to relocation for all data.  $\bar{r}$  indicates the mean residual. (c) Residuals after relocation using all data. (d), (e) as for (b), (c), but showing residuals for relocation using only data at epicentral angles  $<30^\circ$ . (For interpretation of the references to colour in this figure legend, the reader is referred to the web version of this article.)

leading us to suggest that these two earthquakes likely occurred on adjoining segments of the same fault, rather than repeated rupture of the same fault patch. The causative feature must therefore be large enough to sustain a combined moment release equal to a single  $M_w$  5.9 event.

In contrast to the absolute catalogue locations, the smaller 2008 aftershock appears to locate to the northwest, rather than northeast, of the other two events considered, although the degree of the westward shift is poorly constrained (see Fig. 2).

A northwards offset for the 2008 aftershock is common to both the relative and absolute relocations, whereas the direction of the east-west offset changes using the two different techniques. Precise onset times of the direct *P*-wave are difficult to determine

from the waveforms visually, particularly for the lower-amplitude *P*-wave arrivals from the smaller 2008 mainshock, where the onset amplitude is often within the level of the background noise. As a result, the absolute location for this smaller event is less well constrained than for the larger, and hence better resolved earthquakes. We therefore rely on the absolute locations for the 2008 mainshock and 2016 event, and suggest that the 2008 aftershock is somewhere to the north, although its precise location is poorly determined. Any potential causative relationship between the two earthquakes in 2008 is unknown, but if the mechanism relating these two events is assumed to be static stress transfer, then the east-west offset of the aftershock relative to the 2008 mainshock is likely to be less than the northwards offset.

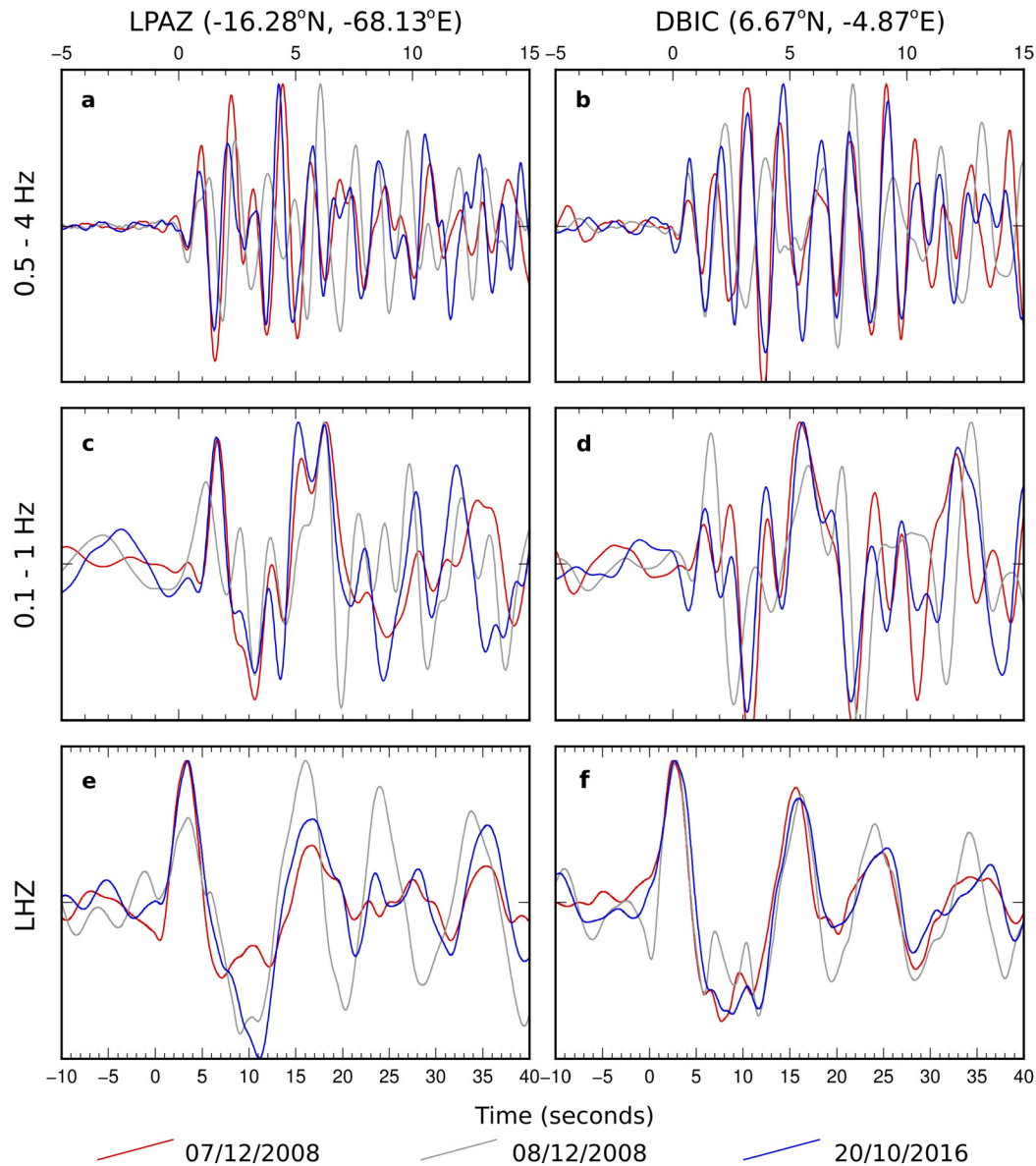


**Fig. 3.** Waveform comparisons at different frequency bands. Left column shows waveforms from station LPAZ in Bolivia. Right column shows waveforms from station DBIC in Cote d'Ivoire. Waveforms aligned relative to *P*-wave arrival. (a, b) Waveforms subject to 4-pole Butterworth filter with pass band 0.5–4 Hz. (c, d) Waveforms subject to 4-pole Butterworth filter with pass band 0.1–1 Hz. (e, f) Waveforms converted to tapered frequency response of a long-period seismometer. (For interpretation of the references to colour in this figure legend, the reader is referred to the web version of this article.)

In the frequency band used for relocation, similarity in overall mechanism and locations of the three earthquakes allow their relative times to be determined. At higher frequencies ( $>1$  Hz), similarity between the waveforms for the two larger events remains apparent, indicating their proximity to one another and similar influence of near-source effects on the waveform. Waveforms for the 2008 aftershock, while similar to the other events at low frequencies, are notably different at higher frequencies, indicating a marginally different rupture process and near-source scattering effects (Fig. 3).

#### 4. Source mechanisms and fault geometry

To supplement the relative and absolute constraints on the earthquake locations, we use teleseismic waveform inversion to constrain the source mechanism, rupture duration and depth for these three earthquakes using *P*- and *SH*-waves, treating each earthquake as a finite-duration point-source centroid.

We invert long-period waveforms observed at teleseismic distances ( $30^{\circ}$ – $80^{\circ}$  epicentral distance) to determine earthquake mechanism parameters, centroid depth, moment, and source duration, using the approach of Zwick et al. (1994). Our method follows that previously used for mid-ocean ridge earthquakes (Huang et al., 1986; Jemsek et al., 1986; Huang and Solomon, 1987), and for the determination of earthquake source parameters in other oceanic settings (Abers, 1991; Abers et al., 1997; Tilmann et al., 2010; Craig et al., 2014). The best-fit parameters for each earthquake are detailed in Table S1. Observed waveforms and best-fit synthetics are shown in Figs. S2–S4.

Fifty seismograms with the best azimuthal distribution were selected, using data available from the Incorporated Research Institutions for Seismology Data Management Center (IRIS DMC). We invert a section of the waveform starting from the initial onset of the direct arrival (manually picked from broadband data), and encompassing the direct arrival (*P*, *S*) and principal depth phases (*pP*, *sP*, *sS*). The inversion window for *P*-waves was limited to ex-

**Table 1**

Mechanism parameters for seismicity near 13°20'N. Values for microseismicity are taken from Parnell-Turner et al. (2017). Values for the three larger earthquakes are based on waveform modelling (this study), shown in Figs. S2–S4.

Identifier	Date & Time	Depth (km bsl)	Moment (N m)	$M_w$	Strike (°)	Dip (°)	Rake (°)
Microseismicity	–	10–14	–	–	352	72	–105
2008 Mainshock	2008/12/07 06:23:10	6.0	$3.555 \times 10^{17}$	5.7	343	52	–104
2008 Aftershock	2008/12/08 01:51:01	5.0	$2.663 \times 10^{17}$	5.6	350	46	–093
2016	2016/10/20 00:09:26	5.1	$4.620 \times 10^{17}$	5.7	345	45	–105

clude subsequent water multiples, and for *S*-waves was limited to exclude any predicted interaction with *SKS* arrivals. Waveforms were weighted in the inversion based on azimuthal density, and *S*-waveforms were manually weighted down by a factor of 0.5 to compensate for their increased amplitude relative to the *P*-wave.

Each earthquake source was parametrised as a finite-duration rupture of a point source, constrained to be a double-couple. The source duration was parametrised as four 1-second elements with independent amplitudes. No improvement in waveform fit was achieved when a longer duration source was tested, and in many cases the final element of the allowed source time function has near-zero amplitude. Hence, for each earthquake we invert for nine parameters: strike, dip, rake, centroid depth, moment, and a four-element source time function.

We use a near-source velocity structure based on the local model derived from a seismic refraction experiment carried out in 2016 in the 13°N area, averaged into a simple half-space (Simão et al., 2016). A water layer is added over the solid Earth structure, with initial thickness from local bathymetry shown in Fig. 1. Small adjustments to the water layer thickness are then made to best match the mean periodicity of observed *P*-wave water multiples. In common with previous work at mid-ocean ridges we find that the inclusion of a Moho, and the transition to faster mantle velocities below it, improves the waveform fit for solutions with sub-Moho depths (Huang et al., 1986; Jemsek et al., 1986; Huang and Solomon, 1987). This approach, however, fails to produce solutions that fit better than those located above the Moho, i.e. within the crust, and we hence present results using the simple half-space model. Routine values of 1 and 4 s (for *P*- and *SH*-waves, respectively) are used for the attenuation parameter  $t^*$  (Futterman, 1962).

Best-fit solutions are plotted in Fig. 1a, and detailed in Table 1 and Figs. S2–S4. Sensitivity tests for depth and dip were performed by fixing the given parameters, and inverting for the best-fit solution. When testing for depth sensitivity, only centroid depth is fixed while all other parameters are free to vary. When testing for dip sensitivity, dip is fixed, centroid depth is fixed at the overall best-fit value, while all other parameters are free to vary. For sensitivity to dip, two minima occur due to the inherent inability to distinguish between the actual fault plane and the conjugate auxiliary plane in the focal mechanism (Figs. 4, 5, and 6).

Centroid depths of all three earthquakes are determined to be within the upper oceanic lithosphere, at depths of <5 km bsl (Figs. 4, 5, 6, and Figs. S2–S4). Forcing the source depth to be >5 km leads to progressively worse fits to the combined *P*- and *SH*-wave dataset (Figs. 4c and 5c). At depths beyond 12 km (2008 mainshock) and 18 km (2016), an east/west-striking thrust-faulting mechanism appears to yield a better fit to the observed waveforms than a north/south-striking normal-faulting mechanism (red points, Figs. 4a and 5a). This thrust faulting mechanism is an artefact of the ability to produce a reduced misfit by fitting the higher amplitude part of the waveform at a subset of stations, whilst minimising the amplitude at others. Although this solution may yield a marginally better overall waveform misfit than a deep normal-faulting mechanism, it fails to fit any identifiable first motion polarities, and cannot produce an acceptable fit to the complete set

of waveforms compared to a normal-faulting earthquake at shallow depths.

Whilst an increased depth can be partially offset by reducing the source duration for an individual phase, the variation in depth-phase delays at different wavespeeds (and subsequent impact on phase overlap) results in a different amplitude dependence for the two phases. This trade-off is shown in Figs. 4b and 5b, which show that although the best-fit model is often able to fit the amplitude of *P*-wave train at moderate depths (~7 km bsl), it then significantly under-predicts the amplitude of the observed *S*-waveform. This shortcoming can be partly overcome by adjusting the elastic parameters used in the inversion, but this results in unrealistic phase separation. Realistic variations in wavespeeds and near-source density produce only 1–2 km variation in global minimum-misfit depth. We therefore conclude that only a shallow source depth is able to fit the amplitudes of both phases simultaneously.

Absolute minimum misfit centroids for all three earthquakes occur at 2–3 km bsl, indicating that rupture likely extended from near the seafloor to depths of ~4–6 km bsl, assuming that earthquakes of this magnitude likely rupture up to (or close to) the seafloor.

Best-fit focal mechanisms for all three earthquakes show north-south striking normal faulting (consistent with routine catalogue results for low-frequency moment tensors), with slip vectors parallel to the regional spreading direction (~110°). Source dip resolution is hampered by the lack of along-strike *SH*-wave data. The best-fit mechanism is achieved, however, with an east-dipping planar dip of ~45° for the 2016 event and a similar value of 52° for the 2008 mainshock (Fig. 2b). The large uncertainty in dip may also reflect the depth-variable dip of the curved detachment fault surface (Figs. 2b and Fig. 3b). The best-fit point-source solution would therefore represent a moment-weighted average of the fault failure surface, and values of ~45–50° would hence be consistent with peak slip at this value in the centre of the rupture patch. Failure would be expected over a range of dip angles either side of this central value, consistent with failure extending from the downdip limit of ~60–65° to the updip limit of ~30–35°.

The point-source approach used here assumes that the causative fault is planar. However, if the source fault is indeed the detachment, then the rupture patch is instead likely to be curved, hence this assumption represents a simplification. However, synthetic waveform tests indicate that moderate down-dip curvature makes little difference to the far-field teleseismic waveforms when compared to a planar-fault model (Braunmiller and Nábělek, 1996). Detection of fault curvature requires both a larger-magnitude earthquake (>  $M_w$  6) and a larger rupture dimension/rupture depth range than those near 13°20'N, to allow the resolution of discrete source orientations within the overall waveform, and also excellent along-strike *SH*-wave coverage. For earthquakes at the Mid-Atlantic Ridge where along-strike coverage is sparse, data are limited to ocean islands, the Atlantic coast of Brazil, and Iceland. While we cannot obtain evidence of down-dip curvature from the waveform data, undetectable curvature of the source fault cannot be ruled out.

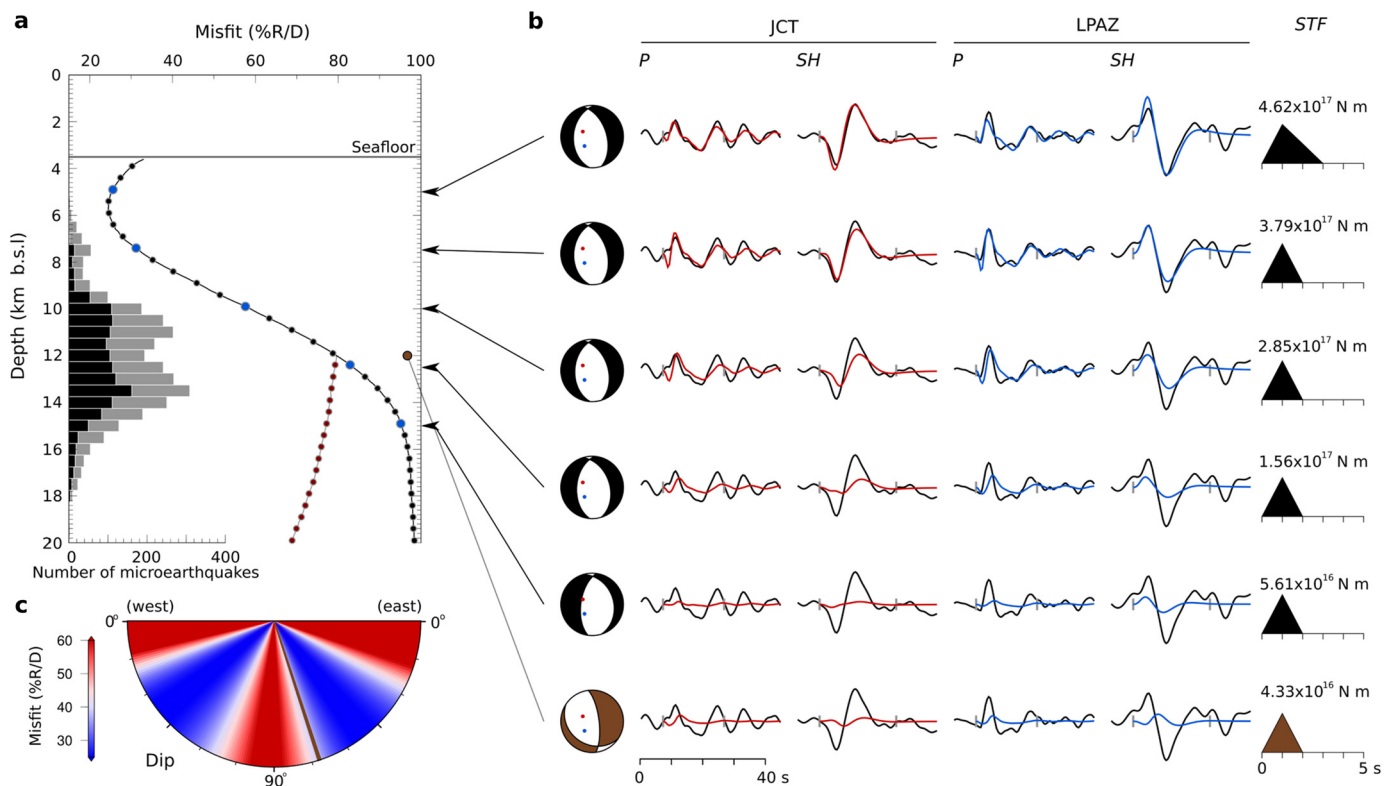


**Fig. 4.** Analysis of 7th December 2008 earthquake. (a) Waveform misfit as a function of depth. Black line/points are for solutions with prior assumption of north-striking normal fault. Blue points indicate depth values used for sensitivity examples shown in b. Grey line/red points are for fully unconstrained solutions. Histograms show depth of extensional microearthquakes from Parnell-Turner et al. (2017), grey for all extensional earthquakes, black for only those adjacent to corrugated dome at 13°20'N. (b) Depth-sensitivity tests at depths of 5, 7.5, 10, 12.5, and 15 km bsl. Left column shows best-fit focal mechanism for each depth interval. Red/blue points show projection of two example stations, JCT and LPAZ, respectively. Following four columns show P- and SH-waveforms for stations JCT and LPAZ. Black traces are observed waveforms, coloured traces are synthetic waveforms for best-fit solution at each depth. Black vertical ticks indicate inversion window. Right hand column shows best-fit source-time function and moment for each depth. Bottom row shows waveforms calculated with depth and mechanism fixed to match values for microearthquake composite mechanism (Parnell-Turner et al., 2017). (c) Dip sensitivity tests. Brown bar shows dip value of composite focal mechanism for normal-faulting microseismicity at base of detachment fault (72°). (For interpretation of the references to colour in this figure legend, the reader is referred to the web version of this article.)

Waveform inversion also yields an estimate of the shape and, of particular interest here, the duration of the source-time function. The estimated duration trades off significantly with depth (see Figs. 4 and 5). However, for both the 2016 event and the 2008 mainshock, the estimated duration for the best-fit model is under 4 s, with the vast majority of the moment release taking place during a 2 s window. As increasing the source depth only serves to shorten the estimated source duration, these estimates represent maximum durations for these events. Rupture propagation speeds for dip-slip earthquakes rarely exceed the local shear-wave speed. Assuming an upper limit on the rupture velocity of 3 km s<sup>-1</sup>, the maximum dimension of the main slip patch is unlikely to exceed 6 km in any direction. The short rupture duration prevents any robust assessment of the rupture direction based on waveform directivity, and hence leaves the orientation of this maximum dimension undetermined.

## 5. Large earthquakes and the 13°20'N OCC

Slip vectors for the 2008 mainshock and 2016 earthquake (shown on Fig. 1b) match to within 5° with the slip azimuth of the exposed fault surface of the OCC, inferred from the trend of surface corrugations (MacLeod et al., 2009; Escartín et al., 2017). A source mechanism and depth matching those derived from microearthquakes cannot adequately match the observed teleseismic waveforms (Fig. 4b, 5b), indicating conclusively that the microseismicity and teleseismic earthquakes are not co-located (Parnell-Turner et al., 2017). We conclude that the depth and source mechanism for these earthquakes is consistent with the failure of the

upper crustal section of the detachment fault between the seafloor and the top of the observed microseismicity (7 km bsf), at moderate dip angles intermediate between the steeply-dipping microseismicity (~72°) and the observed dip of the surface of the exposed fault (14–18°).

At the TAG detachment, shallow seismicity in the footwall (<5 km bsf) has been interpreted as antithetic normal faulting (de-Martin et al., 2007). At 13°20'N, no such faults are evident in microbathymetry of the exposed fault surface (Fig. 1b), nor in the microearthquake catalogue (Parnell-Turner et al., 2017). The distribution of compressional seismicity within the footwall indicates that any bending-related extension in the upper portion of the footwall is probably limited to depths < 2 km below the detachment surface, consistent with the bending of a plate with elastic-plastic rheology (Parnell-Turner et al., 2017). If the  $M_w$  5.7 event was caused by a bending-related extensional fault within the top 2 km of the footwall block, then either the fault must be very long in the along-strike direction, or stress drop must be very high, in order to generate the necessary seismic moment. Given that slip on such faults must gradually decrease to zero as the fault approaches the depth of the neutral surface (2 km), the slip gradient required between 2 km and the surface would therefore be extremely high, and we deem this explanation to be improbable.

Similar arguments apply to the hypothesis that these larger earthquakes result from seismicity within rider blocks that could exist to the east of the breakaway above the footwall. Multibeam bathymetric data show that any rider blocks are restricted to the western part of the 13°20'N OCC near the breakaway (Escartín et al., 2017), and are not on the multiple-km length scale that would

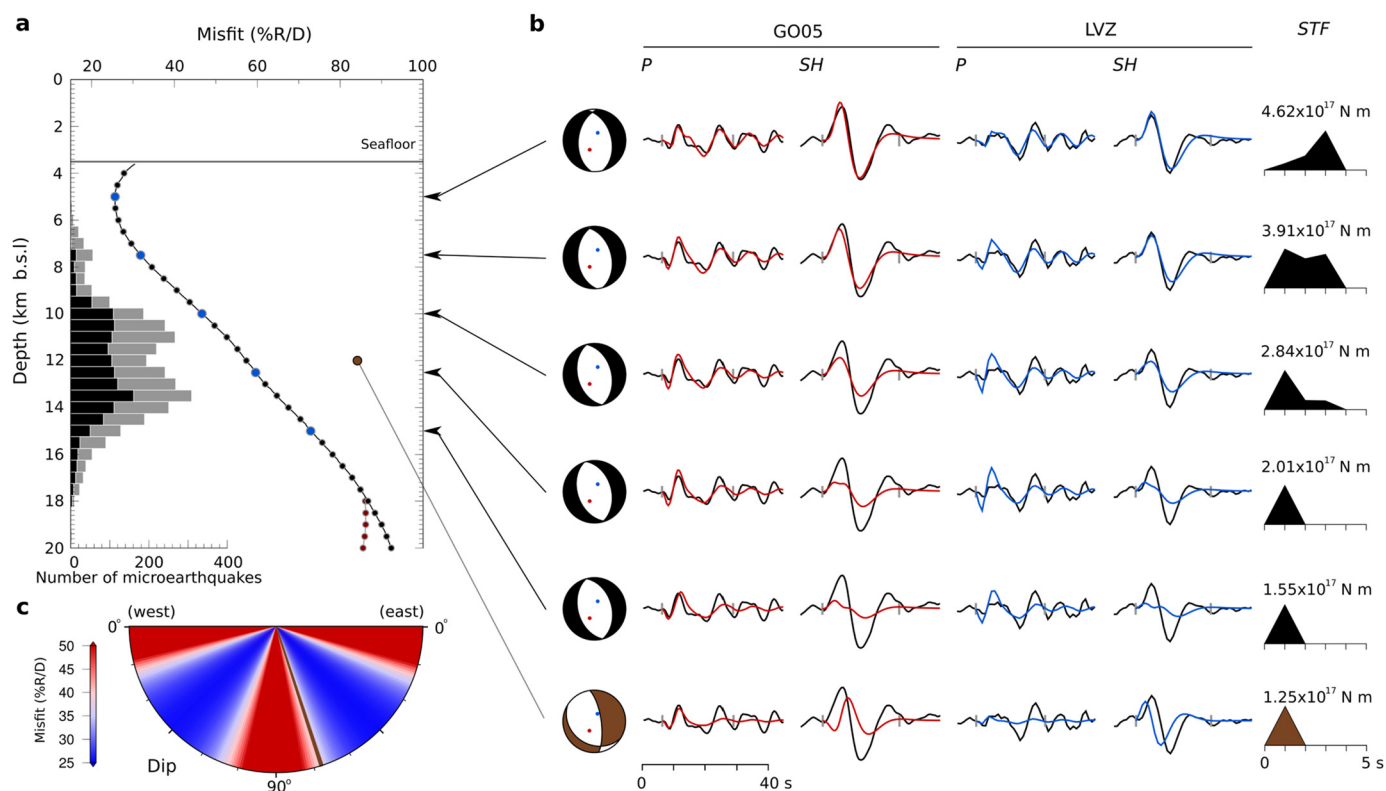


**Fig. 5.** Analysis of 20th October 2016 earthquake. (a) As in Fig. 4. (b) As in Fig. 4, except with stations G005 and LVZ substituted for JCT and LPAZ. (c), (d) As in Fig. 4. (For interpretation of the references to colour in this figure legend, the reader is referred to the web version of this article.)

be required for fault-surfaces to host  $M_w$  5.7 earthquakes without extremely high stress drops. These rider blocks are presumably composed of less coherent hanging wall material which has been subjected to extensive mass wasting, and hence are unlikely to produce major earthquakes.

Two sub-parallel NNE-SSW trending faults, 3 km apart, can be identified in bathymetric data north of the  $13^{\circ}20'N$  OCC, near  $13^{\circ}25'N$ ,  $44^{\circ}55'W$  (Fig. 1). These faults, which are  $\sim 10$  km in length and appear to extend from the western end of the OCC at  $13^{\circ}20'N$  to the probably inactive OCC at  $13^{\circ}30'N$ , could potentially generate earthquakes with a rupture dimension on order  $\sim 5$  km. The dip of the exposed scarps is  $40$ – $50^{\circ}$ , which is compatible with the nodal plane dips for the larger earthquakes, assuming these faults are planar. Deep-tow sidescan sonar data show that these scarps have low-amplitude backscatter, suggesting that they are not smooth exposures of pristine footwall, and instead are covered in mass-wasted material or sediment (MacLeod et al., 2009). This overlying talus would have decreased the dip angle from the true value of the fault at depth, hence these faults may be steeper at depth than they appear on the seabed. These two small faults were within the 2014 OBS network, which failed to detect any clustered microseismicity to indicate these faults are active. Whilst the same is true of the shallow portion of the detachment fault, we would expect to see some degree of microearthquake activity on the areas of the fault surrounding any patch that ruptured in 2008 if one of these faults had hosted a larger earthquake.

The only other major tectonic feature within the axial valley evident in bathymetric data is the eastern rift border fault (Fig. 1a). Placing both the 2016 event and the 2008 mainshock on this feature would require an eastward shift of  $> 10$  km from their globally constrained best-fitting locations. This magnitude of shift is at the limit of both the quantitative catalogue location uncertainty for these earthquakes [NEIC], and typical error in global earthquake location (Lohman and Simons, 2005; Weston et al., 2012). Whilst

we cannot completely rule out this scenario, there is no evidence for systematic westward-bias in the catalogue locations along this section of the Mid-Atlantic Ridge to justify a common shift in both earthquake locations.

## 6. Shallow detachment fault seismogenesis

These results lead us to suggest that the 2008 mainshock and 2016 earthquake most likely occurred on adjoining sections of the detachment fault at  $13^{\circ}20'N$ . The centroid depth and overall mechanism suggest that they ruptured a substantial area of the shallow part of the fault, extending from the near-surface emergence of the fault, down to the presumed limit of the established and contiguous fault plane, constrained by microearthquakes where the fault roots near the brittle-ductile transition.

Using the available constraints on the geometry of the detachment fault, and assuming that the 2016 earthquake and 2008 mainshock did indeed occur on the detachment surface, we can estimate the minimum stress drop for the 2008 mainshock and 2016 earthquake. The maximum area of the detachment fault that can have failed in these two earthquakes is assumed to extend from the seafloor to the upper portion of the detachment-related microseismicity in the down dip direction ( $0$ – $7$  km), and the spreading axis-parallel length over which microearthquakes are observed ( $\sim 15$  km). Over the downdip extent of the fault, we assume uniform curvature from  $30$  to  $70^{\circ}$ . We increase the estimated fault area by 5% to account for the rugosity of the fault plane, based on the three-dimensional surface area calculated for a  $2 \times 2$  km patch of the exposed fault plane using 2m-resolution microbathymetry (Escartín et al., 2017). Hence our estimated total fault area is  $1.3 \times 10^8$  m<sup>2</sup>.

Since the total along-axis extent of the detachment fault exceeds the sum of our estimated maximum rupture dimensions for the 2008 mainshock and the 2016 earthquake, we assume that

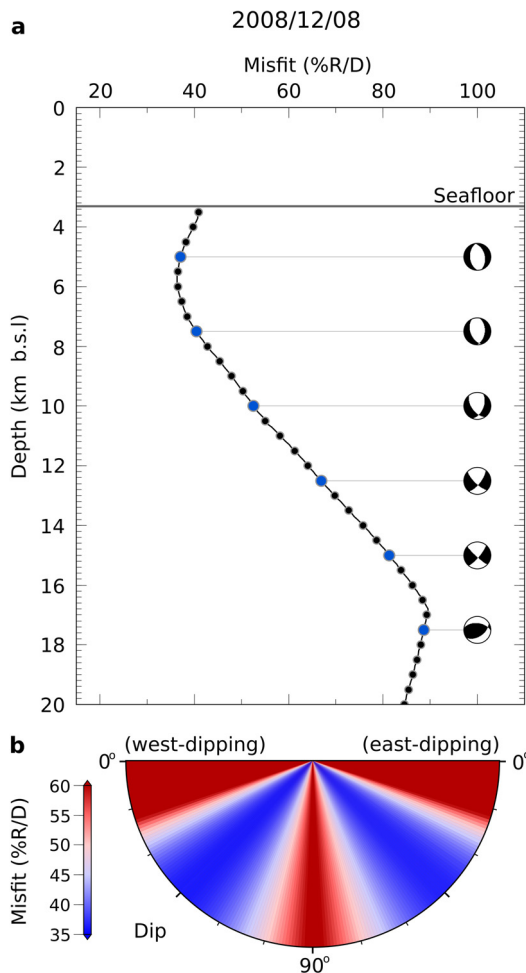


**Fig. 6.** Analysis of 8th December 2008 earthquake. (a) Waveform misfit as a function of depth, calculated at 0.1 km depth intervals. At each depth, best-fit solution is calculated based on free inversion for all source parameters, except depth. Best-fit focal mechanisms shown at 2.5 km increments. (b) Dip sensitivity tests for east-most and west-most dipping planes for 8th December 2008 earthquake. At each dip-value, dip and centroid depth are fixed (at overall best-fit value for centroid depth), while all other parameters vary freely. (For interpretation of the references to colour in this figure legend, the reader is referred to the web version of this article.)

each earthquake ruptured approximately half of the total fault surface available on the 13°20'N detachment (based on their similar magnitudes). We then estimate a minimum stress drop,  $\Delta\sigma$ , for each earthquake by assuming  $\Delta\sigma = cM_0/(A^{3/2})$ , where  $A$  is the fault area,  $M_0$  is the moment, and  $c$  is a geometrical constant, approximately equal to 1. We therefore determine that  $\Delta\sigma \geq 0.68$  MPa for the 2008 mainshock, and  $\Delta\sigma \geq 0.88$  MPa for the 2016 event. These stress drops represent upper bounds, since decreasing the rupture area would increase the stress drop in each earthquake. Nonetheless, these values are consistent with stress drops observed in earthquakes in range of a tectonic regimes (Allmann and Shearer, 2009), and suggest that the detachment fault is capable of sustaining significant shear stresses throughout the upper crust, down to 6 km bsf. Hence this detachment fault appears to be rheologically comparable to globally observed normal-fault systems in non-detachment settings.

It is useful to compare the results presented here with the well-studied system of detachment faults at the western end of the Woodlark Basin, southeastern Papua New Guinea, which is thought to mark the transition from continental extension to oceanic spreading (Little et al., 2007; Wallace et al., 2014). This region contains several active detachment faults and associated core complexes, including the type-examples of the sub-aerial Day-

man Dome, and the sub-marine Moresby Seamount detachment (Spencer, 2010; Speckbacher et al., 2011). Crucially, these faults have been shown to host large-magnitude ( $>M$  6.0), shallowly-dipping normal-faulting earthquakes at shallow depth (Abers, 1991; Abers et al., 1997). Although these detachments are exhuming high-pressure metamorphic rocks in their footwalls, rather than newly-formed igneous oceanic crust, the detachment-faulting process has been suggested to be common to both regimes (e.g. Abers et al., 1997; Little et al., 2007). Despite the presence of large-scale seismicity, recent geodetic work has suggested that much of the slip on these faults is accommodated aseismically through stable sliding on unlocked faults (Wallace et al., 2014), although we note that the proposed coupling models did require locked faults at shallow depth. In common with observations from oceanic detachment systems, these faults are characterised by coincident mylonitization, alteration to phyllosilicate minerals, and widespread precipitation of hydrothermal calcite and quartz, based on in samples dredged from the Moresby Seamount detachment fault (Speckbacher et al., 2011).

Lower-crustal gabbros and mantle peridotites exposed on oceanic detachment footwalls are commonly altered to sheet silicates such as talc and chlorite due to pervasive hydrous circulation (e.g. Dick, 1989; Blackman et al., 2002; Escartín et al., 2003; Karson et al., 2006; Blackman et al., 2014). The presence of these low-friction minerals suggests that within the shallow crust, slip may occur through aseismic creep along a rheologically weak fault surface, implying that the shallow portion of a detachment fault would be unable to support the stresses necessary to produce earthquakes (Escartín et al., 1997; deMartin et al., 2007). In contrast, in-situ sampling of the corrugated dome at 13°20'N shows that, although heavily-altered ultrabasic rocks and talc are present, the exposed fault surface predominantly consists of quartz-cemented cataclastic metadiabase (Bonnemains et al., 2017). These rocks are probably sourced from the hanging wall and later incorporated into the fault zone within the uppermost few kilometres of the crust (Bonnemains et al., 2017). Whilst this zone is unlikely to account for the full rupture area of the larger earthquakes studied here, the migration of rupture into a hanging wall comprised of quartz-cemented breccia suggests that the fault surface must be at least as strong as this material. Hence the fault rheology, even at shallow depths, is not dominated by minerals with low coefficients of static friction – consistent with the presence of shear stresses large enough to produce large earthquakes.

The rheological behaviour of the materials most likely to dominate the fault zone (gabbroic rocks and hydrous alteration products) is highly temperature dependent (e.g. Chernak and Hirth, 2010; Moore and Lockner, 2011). A combination of variable fault rock composition and rheology, the complex thermal structure at the spreading axis, and the unquantified influence of variable pore fluid pressure, fault zone rheology remains highly uncertain. The ability to generate large earthquakes within the uppermost few kilometres of the fault, however, requires that the overall fault rheology in this region be velocity-weakening. It remains unclear why the presence of weak hydrous minerals does not appear to have inhibited seismogenic failure, or had a major weakening effect on the fault itself, at least on the timescale of the earthquake cycle.

At 13°20'N, the apparent occurrence of large-magnitude earthquakes on the shallow part of the detachment fault contrasts with the microseismicity that characterises the deeper, steeper-dipping sections (Fig. 7), and raises questions about what controls the transition in seismogenic character over seemingly short length scales at depth. One important factor is likely to be the thermal profile within the fault zone. However, the thermal structure of oceanic detachment fault systems is difficult to ascertain with any accuracy, as a result of the complex interplay between magmatic processes, the formation of new oceanic lithosphere, and

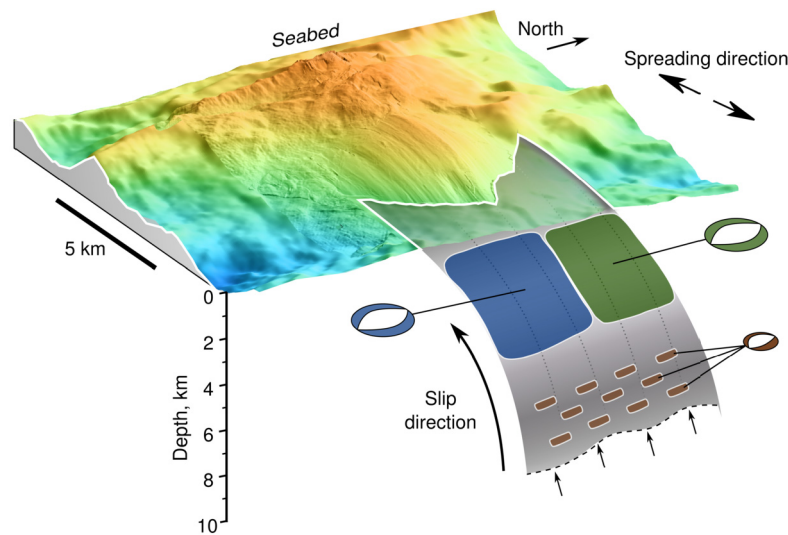


**Fig. 7.** Three-dimensional sketch showing bathymetry and rupture at 13°20'N detachment fault. Grey curved area is portion of detachment fault surface; focal mechanism solutions and rupture patches for 2016 event (blue), 2008 mainshock (green) and subset of microearthquakes (brown) plotted in their expected positions on fault surface. Black arrows show spreading/slip direction. Microbathymetry from (Escartín et al., 2017, French Oceanographic Cruises, <http://dx.doi.org/10.17600/13030070>), with colour shading as in Fig. 1. (For interpretation of the references to color in this figure legend, the reader is referred to the web version of this article.)

widespread hydrothermal percolation, controlled by the local permeability structure. The thermal structure is intrinsically linked to the rheological evolution of the fault zone material, which controls the capacity of the fault zone to sustain stresses. The evolution of the fault itself as the footwall is exhumed may also play a role, since the active fault is thought to emerge from a ductile mylonitic shear zone at depth (Hansen et al., 2013). The fault may develop as strain is localized on many small brittle cracks at intermediate depths, forming as a finite-thickness layer with an anastomosing fabric while generating microearthquakes (Karson et al., 2006; Bonnemains et al., 2017), before coalescing into a single coherent fault zone nearer to the surface. The transition between failure in many microearthquakes to failure in large earthquakes at ~5 km bsf may therefore represent the point at which microcracks coalesce, thus establishing a continuous fault plane, and allowing rupture to propagate continuously over large areas.

Earlier studies of large earthquakes at slow-spreading ridges have shown that teleseismically-detected earthquakes commonly occur with centroid depths of <4 km bsf and at dip angles of 45°, within the uppermost oceanic lithosphere (Huang et al., 1986; Jemsek et al., 1986; Huang and Solomon, 1987). Supra-source water depths from *P*-wave multiples indicate that majority of these larger earthquakes occurred beneath the axial valley, potentially consistent with their occurrence on the down-dip section of detachment faults. However, lacking the bathymetric and microearthquake data to identify active detachment faulting, these poorly-understood events had been assumed to represent slip on rift-bounding border faults. The similarity in dip and depth to the teleseismically-detected earthquakes at 13°20'N suggests that this may not be the case, and instead, slip on the shallow portion of detachment faults may be responsible for many more large earthquakes than previously recognised. This inference is consistent with increased rates of seismic moment release at detachment-dominated spreading segments, and with increased estimates for the thickness of the coupled seismogenic layer (Escartín et al., 2008; Olive and Escartín, 2016).

## 7. Conclusions

We find that large earthquakes at 13°20'N on the MAR are best explained by rupture on the shallow, gently-dipping portion of a detachment fault. At depths of ~10 km bsf, where the fault is pre-

sumed to initiate, a network of local fractures give rise to small magnitude microearthquakes which are undetected by the global teleseismic network. At shallower depths, these smaller rupture patches coalesce into a coherent fault plane, strong enough to produce large earthquakes which rupture substantial portions of the shallow fault surface. Despite the presence of weak minerals and a transition to dip-angles usually thought to be too low to support seismogenic failure, our results show that oceanic detachment faults may be strong, and generate earthquakes in the uppermost ~7 km of the lithosphere, in common with those found on the continents.

## Acknowledgements

TJC thanks the Royal Commission for the Exhibition of 1851 for financial support through a Research Fellowship; RPT was supported by National Science Foundation grant OCE-1458084. Several figures were produced using the Generic Mapping Tools software package. Seismic data were retrieved from the IRIS Data Management Center. We thank Rob Sohn and Javier Escartín for their comments on a draft manuscript, and we thank the editor and two anonymous reviewers for their comments.

## Appendix A. Supplementary material

Supplementary material related to this article can be found online at <http://dx.doi.org/10.1016/j.epsl.2017.09.020>.

## References

- Abers, G.A., 1991. Possible seismogenic shallow-dipping normal faults in the Woodlark-D'Entrecasteaux extensional province, Papua New Guinea. *Geology* 19, 1205–1208.
- Abers, G.A., Mutter, C.Z., Fang, J., 1997. Shallow dips of normal faults during rapid extension: earthquakes in the Woodlark-D'Entrecasteaux rift system, Papua New Guinea. *J. Geophys. Res.* 102, 15301–15317.
- Allmann, B.P., Shearer, P.M., 2009. Global variations of stress drop for moderate to large earthquakes. *J. Geophys. Res.* 114. <http://dx.doi.org/10.1020/2008JB005821>.
- Blackman, D.K., Canales, J.P., Harding, A.J., 2009. Geophysical signatures of oceanic core complexes. *Geophys. J. Int.* 178 (2), 593–613. <http://dx.doi.org/10.1111/j.1365-246X.2009.04184.x>.
- Blackman, D.K., Karson, J.A., Shelly, D.S., Cann, J.R., Früh-Green, G.L., Gee, J.S., Hurst, S.D., John, B.E., Morgan, J., Nooner, S.L., Ross, D.K., Schroeder, T.J., Williams, E.A., 2002. Geology of the Atlantis Massif (Mid-Atlantic Ridge, 30°N): implications

- for the evolution of an ultramafic oceanic core complex. *Mar. Geophys. Res.* 23, 443–469.
- Blackman, D.K., Slagle, A., Guerin, G., Harding, A., 2014. Geophysical signatures of past and present hydration within a young oceanic core complex. *Geophys. Res. Lett.* 41, 1179–1186. <http://dx.doi.org/10.1002/2013GL058111>.
- Bonnemains, D., Escartín, J., Mével, C., Andreani, M., Verlaquet, A., 2017. Pervasive silicification and hangingwall overplating along the 13°20'N oceanic detachment fault (Mid-Atlantic Ridge). *Geochem. Geophys. Geosyst.* 18, 2028–2053. <http://dx.doi.org/10.1002/2017GC006846>.
- Braunmiller, J., Nábělek, J., 1996. Geometry of continental normal faults: seismological constraints. *J. Geophys. Res.* 101, 3045–3052.
- Cann, J.R., Blackman, D.K., Smith, D.K., McAllister, E., Janssen, B., Mello, S., Avgerinos, S., Pascoe, E., 1997. Corrugated slip surfaces formed at ridge-transform intersections on the Mid-Atlantic Ridge. *Nature* 385, 329–332.
- Chernak, L.J., Hirth, G., 2010. Deformation of antigorite serpentinite at high temperature and pressure. *Earth Planet. Sci. Lett.* 296, 23–33.
- Craig, T.J., Copley, A., Jackson, J., 2014. A reassessment of outer-rise seismicity and its implications for the mechanics of oceanic lithosphere. *Geophys. J. Int.* 197, 63–89. <http://dx.doi.org/10.1093/gji/ggu013>.
- deMartin, B.J., Sohn, R.A., Canales, J.P., Humphris, S.E., 2007. Kinematics and geometry of active detachment faulting beneath the Trans-Atlantic Geotraverse (TAG) hydrothermal field on the Mid-Atlantic Ridge. *Geology* 35, 711–714. <http://dx.doi.org/10.1130/G23718A.1>.
- Dick, H.J.B., Tivey, M.A., Tucholke, B.E., 2008. Plutonic foundation of a slow-spreading ridge segment: oceanic core complex at Kane Megamullion, 23°30'N, 45°20'W. *Geochem. Geophys. Geosyst.* 9 (5), Q05014. <http://dx.doi.org/10.1029/2007GC001645>.
- Dick, H.J.B., 1989. Abyssal peridotites, very slow spreading ridges and ocean ridge magmatism. *Geol. Soc. (Lond.) Spec. Publ.* 42, 71–105.
- Escartín, J., Canales, J.P., 2011. Chapman Conference on detachments in oceanic lithosphere: deformation, magmatism, fluid flow and ecosystems. *Eos Trans. AGU* 92, 31. <http://dx.doi.org/10.1029/2011E0040003>.
- Escartín, J., Hirth, G., Evans, B., 1997. Effects of serpentinization on the lithospheric strength and the style of normal faulting at slow-spreading ridges. *Earth Planet. Sci. Lett.* 151 (3–4), 181–189.
- Escartín, J., Mével, C., MacLeod, C.J., McCaig, A.M., 2003. Constraints on deformation conditions and the origin of oceanic detachments: the Mid Atlantic ridge core complex at 15°45'N. *Geochem. Geophys. Geosyst.* 4. <http://dx.doi.org/10.1029/2002GC000472>.
- Escartín, J., Smith, D.K., Cann, J., Langmuir, C.H., Escrig, S., 2008. Central role of detachment faults in accretion of slow-spreading oceanic lithosphere. *Nature* 455.
- Escartín, J., Mével, C., Petersen, S., Bonnemains, D., Cannat, M., Andreani, M., Augustin, N., Bezos, A., Chavagnac, V., Choi, Y., Godard, M., Haaga, K., Hamelin, C., Ildefonse, B., Jamieson, J., John, B., Leleu, T., MacLeod, C.J., Massot-Campos, M., Nomikou, P., Olive, J.A., Paquet, M., Rommevaux, C., Rothenbeck, M., Steinführer, A., Tominaga, M., Triebe, L., Campos, R., Gracías, N., Garcia, R., 2017. Tectonic structure, evolution and the nature of oceanic core complexes and their detachment fault zones (13°20'N and 13°30'N, Mid Atlantic Ridge). *Geochem. Geophys. Geosyst.* 18. <http://dx.doi.org/10.1002/2016GC006775>.
- Futterman, W.I., 1962. Dispersive body waves. *J. Geophys. Res.* 67, 5279–5291.
- Grevemeyer, I., Reston, T.J., Moeller, S., 2013. Microseismicity of the Mid-Atlantic Ridge at 7°–8°15' S and at the Logatchev Massif oceanic core complex at 14°40'N–14°50'N. *Geochem. Geophys. Geosyst.* 14, 3532–3554. <http://dx.doi.org/10.1002/ggge.20197>.
- Hansen, L.N., Cheadle, M.J., John, B.E., Swapp, S.M., Dick, H.J.B., Tucholke, B.E., Tivey, M.A., 2013. Mylonitic deformation at the Kane oceanic core complex: implications for the rheological behaviour of oceanic detachment faults. *Geochem. Geophys. Geosyst.* 14. <http://dx.doi.org/10.1002/ggge.20184>.
- Huang, P.Y., Solomon, S.C., 1987. Centroid Depths and Mechanisms of Mid-Ocean Ridge Earthquakes in the Indian, Gulf of Aden, and Red Sea. *J. Geophys. Res.* 92, 1361–1382.
- Huang, P.Y., Solomon, S.C., Bergman, E.A., Nabelek, J.L., 1986. Focal Depths and Mechanisms of Mid-Atlantic Ridge Earthquakes from Body Waveform Inversion. *J. Geophys. Res.* 91, 579–598.
- International Seismological Centre, 2014. On-line bulletin. *Int. Seis. Cent.*, Thatcham, United Kingdom. <http://www.isc.ac.uk>.
- Jemsek, J.P., Bergman, E.A., Nabelek, J.L., Solomon, S.C., 1986. Focal depths and mechanisms of large earthquakes on the arctic mid-ocean ridge system. *J. Geophys. Res.* 91, 13993–14005.
- Karson, J.A., Früh-Green, G.L., Kelley, D.S., Williams, E.A., Yoerger, D.R., Jakuba, M., 2006. Detachment shear zone of the Atlantis Massif core complex, Mid-Atlantic Ridge, 30°N. *Geochem. Geophys. Geosyst.* 7. <http://dx.doi.org/10.1029/2005GC001109>.
- Kong, L.S.L., Solomon, S.C., Purdy, G.M., 1992. Microearthquake characteristics of a mid-ocean ridge along-axis high. *J. Geophys. Res.* 97, 1659–1685.
- Little, T.A., Baldwin, S.L., Fitzgerald, P.G., Montelone, B., 2007. Continental rifting and metamorphic core complex formation ahead of the Woodlarkspreading ridge, D'Entrecasteaux Islands, Papua New Guinea. *Tectonics* 26. <http://dx.doi.org/10.1029/2005TC001911>.
- Lohman, R.B., Simons, M., 2005. Locations of selected small earthquakes in the Zagros mountains. *Geochem. Geophys. Geosyst.* 6. <http://dx.doi.org/10.1029/2004GC000849>.
- MacLeod, C.J., Escartín, J., Banerji, D., Banks, G.J., Gleeson, M., Irving, D.H.B., Lilly, R.M., McCaig, A.M., Niu, Y., Allerton, S., Smith, D.K., 2002. Direct geological evidence for oceanic detachment faulting: the Mid-Atlantic Ridge, 15°45'N. *Geology* 30, 879–888.
- MacLeod, C.J., Searle, R.C., Murton, B.J., Casey, J.F., Mallows, C., Unsworth, S.C., Achenback, K.L., Harris, M., 2009. Life cycle of oceanic core complexes. *Earth Planet. Sci. Lett.* 287, 333–344. <http://dx.doi.org/10.1016/j.epsl.2009.08.016>.
- Mallows, C., Searle, R.C., 2012. A geophysical study of oceanic core complexes and surrounding terrain, Mid-Atlantic Ridge 13°–14°N. *Geochem. Geophys. Geosyst.* 13. <http://dx.doi.org/10.1029/2012GC004075>.
- Moore, D.E., Lockner, D.A., 2011. Frictional strengths of talc-serpentine and talc-quartz mixtures. *J. Geophys. Res.* 116. <http://dx.doi.org/10.1029/2010JB007881>.
- Morris, A., Gee, J.S., Pressling, N., John, B.E., MacLeod, C.J., Grimes, C.B., Searle, R.C., 2009. Footwall rotation in an oceanic core complex quantified using reoriented Integrated Ocean Drilling Program core samples. *Earth Planet. Sci. Lett.* 287, 217–228. <http://dx.doi.org/10.1016/j.epsl.2009.08.007>.
- Olive, J.-A., Escartín, J., 2016. Dependence of seismic coupling on normal fault style along the Northern Mid-Atlantic Ridge. *Geochem. Geophys. Geosyst.* 17, 4128–4152. <http://dx.doi.org/10.1002/2016GC006460>.
- Parnell-Turner, R., Sohn, R.A., Peirce, C., Reston, T.J., Macleod, C.J., Searle, R.C., Simão, N.M., 2017. Oceanic detachment faults generate compression in extension. *Geology*. <http://dx.doi.org/10.1130/G39232.1>.
- Simão, N., Peirce, C., Falder, Matthew, Reston, T.J., Macleod, C.J., Searle, R.C., 2016. Velocity structure of the crust at 13°N on the Mid-Atlantic Ridge: implications for crustal accretion and oceanic core complex formation. Abstract T33A-2997 presented at 2016 Fall Meeting, AGU, San Francisco, Calif. 12–16 Dec.
- Smith, D.K., Cann, J.R., Escartín, J., 2006. Widespread active detachment faulting and core complex formation near 13°N on the Mid-Atlantic Ridge. *Nature* 442, 440–443.
- Solomon, S.C., Huang, P.Y., 1987. Centroid depths and mechanisms of mid-ocean ridge earthquakes in the Indian Ocean, Gulf of Aden, and Red Sea. *J. Geophys. Res.* 92, 1361–1382.
- Speckbacher, R., Behrmann, J.H., Nagel, T.J., Stipp, M., Devey, C.W., 2011. Splitting a continent: insight from submarine high-resolution mapping of the Moresby Seamount detachment, offshore Papua New Guinea. *Geology* 39, 651–654. <http://dx.doi.org/10.1130/G31931.1>.
- Spencer, J.E., 2010. Structural analysis of three extensional detachment faults with data from the 2000 Space-Shuttle Radar Topography Mission. *GSA Today* 20, 4–10.
- Sykes, L.R., 1967. Mechanism of earthquakes and nature of faulting on the mid-ocean ridges. *J. Geophys. Res.* 72, 2131–2153.
- Tilmann, F.J., Craig, T.J., Grevemeyer, I., Suwargadi, B., Kopp, H., Flueh, E., 2010. The updip seismic/aseismic transition of the Sumatra megathrust illuminated by aftershocks of the 2004 Aceh-Andaman and 2005 Nias events. *Geophys. J. Int.* 181, 1261–1274. <http://dx.doi.org/10.1111/j.1365-246X.2010.04597.x>.
- Toomey, D.R., Solomon, S.C., Purdy, G.M., Murray, M.H.H., 1985. Microearthquakes beneath the median valley of the Mid-Atlantic Ridge near 23°N: hypocenters and focal mechanisms. *J. Geophys. Res.* 90, 5443–5458.
- Tucholke, B.E., Lin, J., Kleinrock, M.C.C., 1998. Megamullions and mullion structure defining oceanic metamorphic core complexes on the Mid-Atlantic Ridge. *J. Geophys. Res.* 103, 9857–9866.
- Wallace, L.M., Ellis, S., Tregoning, P., Palmer, N., Rosa, R., Stanaway, R., Oa, J., Nidkumbu, E., Kwazi, J., 2014. Continental breakup and UHP rock exhumation in action: GPS results from the Woodlark Rift, Papua New Guinea. *Geochem. Geophys. Geosyst.* 15, 4267–4290. <http://dx.doi.org/10.1002/2014GC005458>.
- Weston, J., Ferreira, A.G., Funning, G.J., 2012. Systematic comparisons of earthquake source models determined using InSAR and seismic data. *Tectonophysics* 532–535, 61–81. <http://dx.doi.org/10.1016/j.tecto.2012.02.001>.
- Wolfe, C.J., Purdy, G.M., Toomet, D.R., Solomon, S.C., 1995. Microearthquake characteristics and crustal velocity structure at 29°N on the Mid-Atlantic Ridge: the architecture of a slow spreading segment. *J. Geophys. Res.* 100, 24449–24472.
- Zwicky, P., McCaffrey, R., Abers, G., 1994. MT5 program. IASPEI Software Library 4.



## Corrigendum

## Corrigendum to “Depth-varying seismogenesis on an oceanic detachment fault at 13°20′N on the Mid-Atlantic Ridge” [Earth Planet. Sci. Lett. 479 (2017) 60–70]



Timothy J. Craig<sup>a,\*</sup>, Ross Parnell-Turner<sup>b</sup>

<sup>a</sup> Institute of Geophysics and Tectonics, School of Earth and Environment, University of Leeds, Leeds, LS2 9JT, UK

<sup>b</sup> Department of Geology and Geophysics, Woods Hole Oceanographic Institution, Woods Hole Road, Woods Hole, MA 02543, USA

### ARTICLE INFO

#### Article history:

Received 26 March 2018

Accepted 26 March 2018

Available online 11 April 2018

Editor: R. Bendick

The microseismic hypocenters plotted in our study, derived in Parnell-Turner et al. (2017), used data collected by instrumentation from the NERC Ocean-Bottom Instrumentation Facility (Minshull et al., 2005) under the auspices of NERC projects NE/J022551/1, NE/J02029X/1 and NE/J021741/1 led by Tim Reston, Christine Peirce and Christopher MacLeod, during cruises JC102 and JC109 led by Christine Peirce. The raw seismic data from the OBS deployment are available from the NERC's British Oceanographic Data Centre (<https://www.bodc.ac.uk>), or by contacting the NERC grant-holders directly.

### References

- Minshull, T.A., Sinha, M.C., Peirce, C., 2005. Multi-disciplinary, sub-seabed geophysical imaging – a new pool of 28 seafloor instruments in use by the United Kingdom Ocean Bottom Instrument Consortium. *Sea Technol.* 46 (10), 27–31.
- Parnell-Turner, R., Sohn, R.A., Peirce, C., Reston, T.J., MacLeod, C.J., Searle, R.C., Simão, N.M., 2017. Oceanic detachment faults generate compression in extension. *Geology*. <https://doi.org/10.1130/G39232.1>.

DOI of original article: <https://doi.org/10.1016/j.epsl.2017.09.020>.

\* Corresponding author.

E-mail address: [t.j.craig@leeds.ac.uk](mailto:t.j.craig@leeds.ac.uk) (T.J. Craig).